scientific reports

Check for updates

OPEN

The combination of the ^{18}F-FDG PET and susceptibility-weighted imaging for diagnosis of cerebral glucose metabolism and iron deposition in Parkinson's disease

Zhibing He[1,4], Chao Yang[1,5], Ling Zhou[4,5] & Shuang Li[1,2,3]✉

This study aimed to evaluate the diagnostic potential of combining ^{18}F-FDG PET and susceptibility-weighted imaging (SWI) to assess cerebral glucose metabolism and iron deposition patterns in Parkinson's disease (PD), and to determine their correlations with clinical progression and diagnostic accuracy. Forty-nine PD patients and 70 age-/sex-matched healthy controls underwent standardized ^{18}F-FDG PET and SWI. Metabolic activity (SUVR) and SWI phase values were quantified in cortical/subcortical regions. Statistical analyses included Mann–Whitney U tests, Pearson/Spearman correlations, and ROC curve analysis to evaluate biomarker-clinical relationships and diagnostic performance. PD patients exhibited hypometabolism in frontal, parietal, and temporal cortices ($P < 0.05$) and hypermetabolism in the putamen, globus pallidus, and cerebellum ($P < 0.05$). Cortical hypometabolism correlated with Hoehn-Yahr (H-Y) stages (e.g., temporal lobe: $r = -0.405$, $P = 0.004$) and UPDRS III scores (e.g., frontal cortex: $r = -0.364$, $P = 0.011$). SWI revealed reduced phase values in the substantia nigra, red nucleus, and basal ganglia ($P < 0.001$), with substantia nigra phase values strongly correlating with H-Y stages ($r = -0.525$) and UPDRS III scores ($r = -0.446$). Multimodal integration of ^{18}F-FDG PET and SWI achieved superior diagnostic accuracy (AUC = 0.844) compared to single-modality models (PET: AUC = 0.777; SWI: AUC = 0.780, $P < 0.0001$). The integration of ^{18}F-FDG PET and SWI enhances PD diagnosis by capturing complementary metabolic and iron deposition biomarkers. Cortical hypometabolism may precede subcortical iron accumulation, aligning with Braak staging theory. Limitations include cross-sectional design and technical constraints in SWI quantification. Future studies should validate these findings with longitudinal cohorts and advanced techniques like QSM.

Keywords Parkinson's disease, ^{18}F-FDG PET, Susceptibility-weighted imaging, Multimodal biomarkers, Diagnostic accuracy, Iron deposition

Parkinson's disease (PD) is a neurodegenerative disorder characterized by the primary pathological feature of the loss of dopaminergic neurons in the substantia nigra, leading to reduced axonal projections to the striatum[1–4]. The classic motor features of bradykinesia, rigidity, resting tremor, and postural instability are recognized as the cornerstone of several clinical diagnostic criteria in PD[5,6]. However, the diagnosis of PD remains challenging due to overlapping clinical features with other neurodegenerative conditions. Even for experts in movement disorders, only 58% of patients in the early stages of clinical disease (< 5 years since onset of motor symptoms) are accurately diagnosed[7]. Therefore, developing reliable in vivo biomarkers for early and accurate diagnosis is crucial for future disease-modifying therapies in PD[8,9].

[1]Department of Nuclear Medicine, Xiangyang No. 1 People's Hospital, Hubei University of Medicine, 15 Jiefang Road, Fan District, Xiangyang 441000, Hubei, China. [2]Hubei Provincial Clinical Research Center for Parkinson's Disease Xiangyang No.1 People's Hospital, Hubei University of Medicine, Xiangyang 441000, Hubei, China. [3]Hubei Province Key Laboratory of Molecular Imaging, Wuhan 430022, China. [4]Department of Radiology, Xiangyang No. 1 People's Hospital, Hubei University of Medicine, Xiangyang, China. [5]Chao Yang and Ling Zhou contributed equally to this work. ✉email: 284631445@qq.com

In recent years, various neuroimaging modalities have been employed to provide objective biomarkers for assessing the underlying pathology in PD[10,11]. Positron emission tomography/computed tomography (PET/CT) is a powerful hybrid imaging technique that allows noninvasive tracking of brain pathophysiological processes in neurological and psychiatric disorders[12,13]. [18F]-fluorodeoxy-glucose (^{18}F-FDG), which measures brain metabolism, has shown promise in evaluating metabolic disorders, including PD. As the most widely used radiotracer for cerebral glucose metabolism, ^{18}F-FDG reflects neuronal function and reveals disease-specific changes due to synaptic dysfunction, neuronal degeneration, and compensatory network alterations[14,15]. Consequently, ^{18}F-FDG PET has become a key diagnostic tool for neurodegenerative disorders[16,17].

Susceptibility-weighted imaging (SWI) has also emerged as a valuable technique for detecting iron accumulation in the basal ganglia, a pathological feature associated with dopaminergic neuron loss[18,19]. However, the relationship between these imaging markers and disease progression remains unclear, and whether combining these markers enhances diagnostic specificity is still an open question. Previous studies have largely examined ^{18}F-FDG PET and SWI for distinguishing between PD and multiple system atrophy and progressive supranuclear palsy[20,21]. This leaves unresolved questions about the interplay between metabolic and iron deposition changes in PD pathogenesis.

Early and precise PD diagnosis is vital for the future development of disease-modifying treatments. This study addresses three key unanswered questions: First, whether regional metabolic abnormalities in PD measured by ^{18}F-FDG PET exhibit differential correlations with motor severity (UPDRS III) and disease staging (Hoehn & Yahr stage). Second, how SWI-derived phase values in iron-rich nuclei correlate with clinical progression metrics. Third, whether combining FDG metabolic and iron-sensitive imaging parameters improves diagnostic accuracy compared to single-modality approaches. By employing rigorous quantitative analyses in age- and gender-matched PD and healthy control cohorts, we systematically evaluate FDG metabolic profiles, basal ganglia iron deposition patterns, and multimodal biomarker interactions. Our findings provide novel insights into the neuroimaging signatures of PD progression and establish a framework for optimizing diagnostic algorithms through biomarker integration.

Materials and methods

Participants

Forty-nine patients with Parkinson's disease (PD) (25 males, 24 females; mean age 60.3 ± 10.8 years) meeting the Movement Disorder Society clinical diagnostic criteria[22] were prospectively enrolled from January 2022 to June 2024 at Xiangyang No.1 People's Hospital, Hubei University of Medicine. All patients underwent standardized ^{18}F-FDG PET and SWI protocols. A sex- and age-matched healthy control cohort (n = 70; 38 males, 32 females; mean age 62.6 ± 9.3 years) was recruited through routine health screenings, excluding individuals with neurological/psychiatric histories or substance use disorders. This retrospective study was conducted in accordance with the Declaration of Helsinki (2013 revision). The study received approval from the Institutional Review Board of Xiangyang No.1 People's Hospital (No. [2024SXJS-010]). Written informed consent was obtained from each participant or their authorized legal representative prior to the PET/CT and MRI scan. All PD patients underwent a comprehensive neurological examination, including assessment using the Unified Parkinson's Disease Rating Scale (UPDRS) and Hoehn-Yahr (H-Y) stage, performed by two movement disorder experts. Neurological examinations, SWI, and PET scans were conducted in the drug-off state, with participants refraining from taking any antiparkinsonian medications for at least 12 h prior to the tests. Cognitive function in PD patients was evaluated using the Mini-Mental State Examination (MMSE) and Montreal Cognitive Assessment (MoCA) during the drug-on state.

Data acquisition

All participants underwent imaging examinations using a PET/CT scanner (uMI780, Shanghai, China) and a 3.0-T MRI scanner (Siemens Magnetom Vida). Prior to the ^{18}F-FDG PET examination, participants were instructed to fast for at least 6 h and ensure their fasting blood glucose level was ≤ 6.0 mmol/L. Following the intravenous injection of ^{18}F-FDG (radiochemical purity > 98%) at a dose of 3.7 MBq/kg body weight, participants were asked to rest quietly for 40–60 min. PET images were acquired using the time-of-flight (TOF) and the ordered subset expectation maximization (OSEM) algorithm with the following parameters: data acquisition time window of 10 min, matrix size of 128 × 128, slice thickness of 2.44 mm, 4 iterations, 20 effective subsets, and a full width at half maximum (FWHM) of 3.0 mm. For SWI, the following parameters were used: repetition time (TR) of 28 ms, echo time (TE) of 20 ms, slice thickness of 1 mm, and field of view (FoV) of 179 × 230 mm.

Quantitative analysis of ^{18}F-FDG PET images

The ^{18}F-FDG PET image analysis was performed using MM BrainAnalysis software (Shanghai United Imaging Intelligence Co., Ltd.) to analyze data from all cases. Firstly, intelligent brain segmentation was performed on the 3D T1 MRI sequence. The T1 images were segmented into gray matter, white matter, and cerebrospinal fluid, which were then further segmented into 106 brain regions. Subsequently, map the segmentation results of T1 onto the PET images. After the alignment process, the mean standardized uptake value (SUVmean) was extracted for each cerebral cortex[23]. The cerebellum on the same side was used as the background to calculate the standard uptake value ratio (SUVR) for the ROIs.

Quantitative analysis the phase map of SWI images

On the post-processing workstation, two physicians with 5 years or more of experience in neural system imaging diagnosis jointly performed visual assessment of SWI images in a blinded manner. They manually delineated the ROIs for the bilateral caudate, putamen, globus pallidus, substantia nigra, and red nucleus on the layers displayed clearly in the Phase Map of SWI imaging, measuring the phase values.

Clinical features	PD	HC	χ^2/t/Z	P
Participants	49	70		
Age (years)	60.3 ± 10.8	62.6 ± 9.3	− 0.867	0.386
Gender (M/F)	25/24	38/32	0.123	0.852
Disease duration(years)	2.604 ± 1.59	–		
UPDRS III	22.00 ± 9.36	–		
H-Y stage	2.061 ± 0.80	–		
MMSE	27.533 ± 3.03	–		
MoCA	23.533 ± 4.83	–		

Table 1. The study examined the demographic and clinical characteristics of all participants. The data are presented as mean ± standard deviation. PD, Parkinson's disease; HC, healthy control; F, female; M, male; UPDRS III, motor score of unified Parkinson's Disease rating scale; H-Y stage, Hoehn-Yahr stage; MMSE, Mini-Mental State Examination; MoCA, Montreal Cognitive Assessment.

Region	PD SUVR	HC SUVR	t / Z	P
Frontal cortex	1.137 ± 0.13	1.536 ± 0.32	− 6.649	< 0.0001*
Parietal cortex	1.112 ± 0.11	1.492 ± 0.31	− 8.271	< 0.0001*
Temporal cortex	0.975 ± 0.14	1.273 ± 0.30	− 5.893	< 0.0001*
Globus pallidus	1.064 ± 0.19	0.981 ± 0.08	− 2.946	0.004*
Putamen	1.490 ± 0.28	1.361 ± 0.15	− 2.956	0.004*
Thalamus	1.104 ± 0.09	1.162 ± 0.18	− 1.566	0.117
Pons	0.832 ± 0.10	0.846 ± 0.15	− 0.373	0.709
Cerebellum	6.061 ± 1.32	5.309 ± 0.84	− 3.231	0.001*

Table 2. Comparative analysis of the SUVR of ^{18}F-FDG PET imaging in HC individuals and patients with PD. The data are presented as mean ± standard deviation. HC, healthy control; PD, Parkinson's disease; SUVR, standardized uptake value rate. *Statistically significant with $P < 0.05$.

Statistical analysis

The statistical analysis comprised the utilization of the Mann–Whitney U test for non-normally distributed quantitative data and the independent sample t-test for normally distributed data. Chi-squared tests were applied for categorical data. Pearson correlation or Spearman's rank correlation analysis was conducted to explore the correlation between the ^{18}F-FDG and SWI phase values with H&Y stages and UPDRS III scores in PD patients. Additionally, receiver operating characteristic (ROC) curve analysis was employed to assess the predictive models for PD diagnosis using the ^{18}F-FDG PET model and the phase value of SWI model, as well as the combined models. All statistical analyses were performed using SPSS software (version 25.0). A two-tailed *P*-value of less than 0.05 was considered to indicate statistical significance.

Results

Demographic data and clinical profiles

A total of 119 subjects, including 49 PD subjects (mean age 60.3 ± 10.8y) and 70 HC subjects (mean age 62.6 ± 9.3y), were enrolled. In the PD group, 41.2% (25/49) were male, while in the HC group, 58.8% (38/70) were male. No significant differences were observed between the two groups in terms of gender ($\chi^2 = 0.123$, $v = 1$, $P = 0.852$) and age ($Z = -0.867$, $P = 0.386$). The patients with PD had no obvious dementia: the mean score of MMSE and MoCA was 27.533 ± 3.03 and 23.533 ± 4.83, respectively. (Table1).

The results of quantitative analysis in ^{18}F-FDG PET imaging

In comparison to HC individuals, patients with PD demonstrated a significant reduction in metabolic activity in the frontal ($Z = 6.649$, $P < 0.0001$), parietal ($t = -8.271$, $v = 117$, $P < 0.0001$) and temporal cortices ($Z = -5.893$, $P < 0.0001$). And showed notably increased metabolism in the putamen ($t = -2.956$, $v = 117$, $P = 0.004$), globus pallidus ($t = -2.946$, $v = 117$, $P = 0.004$), and cerebellum ($Z = -3.231$, $P = 0.001$) than in the HC individuals. The quantitative analysis results from ^{18}F-FDG PET imaging are presented in Table 2 and Fig. 1.

Furthermore, the study aimed to examine the relationship between ^{18}F-FDG uptake, H-Y stages, and UPDRS III scores. Figure 2 illustrates the negative correlation between metabolic activity in the frontal cortex ($r = -0.327$, $P = 0.022$), parietal cortex ($r = -0.297$, $P = 0.038$), temporal lobe ($r = -0.405$, $P = 0.004$), globus pallidus ($r = -0.390$, $P = 0.006$), thalamus ($r = -0.358$, $P = 0.012$), pons ($r = -0.367$, $P = 0.010$), and cerebellum ($r = -0.364$, $P = 0.005$) in relation to H-Y stages. In contrast, no significant correlation was observed in the putamen ($r = -0.146$, $P = 0.318$). Additionally, a negative correlation was found between metabolic activity in the frontal cortex ($r = -0.364$, $P = 0.011$), parietal cortex ($r = -0.309$, $P = 0.033$), temporal lobe ($r = -0.310$, $P = 0.032$), thalamus ($r = -0.301$, $P = 0.038$), and cerebellum ($r = -0.394$, $P = 0.005$) with UPDRS III scores. Similarly, no

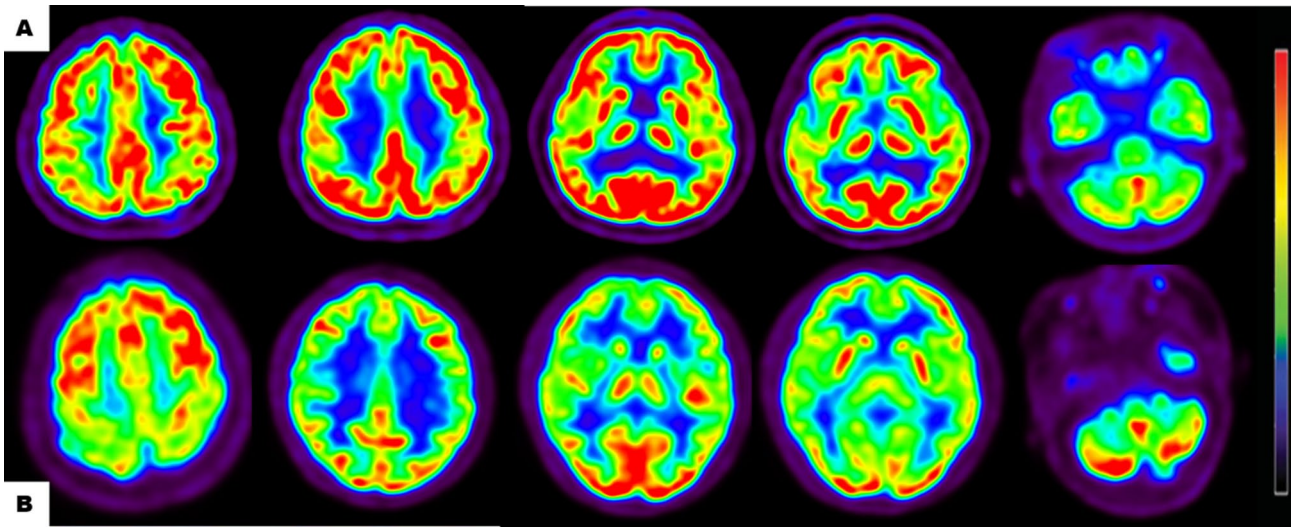

Fig. 1. The images presented depict ^{18}F-FDG uptakes in PET imaging of HC individual (**A**) and patient with PD (**B**). (**A**) HC group individual, man, 68 years. The ^{18}F-FDG PET imaging show a symmetric distribution pattern of the cerebral cortex and nigrostriatal regions, with no apparent areas of increased or decreased radioactive uptake, or mild frontal cortex metabolic reduction caused by normal aging. (**B**) A 74-year-old male with PD. The FDG PET imaging revealed local cortical metabolism reduction in the frontal, parietal, or temporal cortical regions, and increased metabolism in the cerebellum.

significant correlations were observed in the putamen ($r=-0.028$, $P=0.848$), globus pallidus ($r=-0.261$, $P=0.073$), pons ($r=-0.249$, $P=0.088$), and cerebellum ($r=-0.250$, $P=0.086$).

The results of SWI quantitative analysis

Table 3 presents the SWI phase values for both the PD and HC groups. The PD group exhibited significantly lower phase values in the bilateral caudate ($t=-8.046$, $v=117$, $P<0.0001$), putamen ($t=-6.662$, $v=117$, $P<0.0001$), globus pallidus ($Z=-6.652$, $P<0.0001$), substantia nigra ($t=-2.132$, $v=117$, $P=0.035$), and red nucleus ($Z=-6.091$, $P<0.0001$) compared to the HC group. The lowest phase values in SWI were observed in the bilateral substantia nigra (-22.105 ± 43.67 vs. 0.703 ± 65.33), followed by the red nucleus (17.459 ± 33.60 vs. 29.720 ± 40.05), globus pallidus (2.912 ± 44.05 vs. 66.182 ± 43.35), putamen (4.835 ± 31.13 vs. 42.009 ± 29.11), and caudate (14.083 ± 32.08 vs. 54.261 ± 22.31), as depicted in Figs. 3 and 4.

Furthermore, the investigation extended to exploring the correlation between SWI phase values and H&Y stages and UPDRS III scores. Phase values in the substantia nigra ($r=-0.525$, $P<0.001$), and red nucleus ($r=-0.404$, $P<0.001$) were measured, revealing a negative correlation with H-Y stages. In contrast, no significant correlation was observed in the globus pallidus, putamen, and caudate (all $P>0.05$). Additionally, a negative correlation was found between phase values in the substantia nigra ($r=-0.446$, $P<0.001$) with UPDRS III scores. Similarly, no significant correlations were observed in the red nucleus, globus pallidus, putamen, and caudate (all $P>0.05$) , as illustrated in Fig. 5.

The combined analysis of ^{18}F- FDG uptake in cerebral cortical regions and phase values from SWI in patients with PD

Figure 6 presents the ROC curves for diagnosing patients with PD, the combination of the ^{18}F-FDG and SWI phase values model exhibited the highest reliable prognostic performance, yielding an area under the curve (AUC) of 0.844 (95% confidence interval [0.821–0.867], $P<0.0001$). The diagnostic performance of the combination models was significantly higher than that of ^{8}F-FDG model (AUC = 0.777) and SWI phase values (AUC = 0.780) model (all $P<0.0001$).

Discussion

This study systematically elucidates the spatial distribution characteristics and clinical correlations of cerebral glucose metabolism abnormalities and iron deposition in PD through the integration of ^{18}F-FDG PET and SWI technologies. It is the first to validate the enhanced diagnostic efficacy of multimodal imaging biomarker combinations for PD. The findings not only deepen the understanding of PD pathophysiological mechanisms but also provide critical evidence for optimizing biomarker selection in clinical practice.

Complementarity of multimodal imaging and pathophysiological insights

The integration of ^{18}F-FDG PET and SWI achieved superior diagnostic performance (AUC = 0.844) compared to single-modality approaches (PET AUC = 0.777; SWI AUC = 0.780), highlighting the complementary value of multimodal imaging in PD. This enhanced efficacy has dual theoretical implications. First, metabolic abnormalities and iron deposition appear to represent distinct yet interconnected dimensions of PD progression[24]. Specifically,

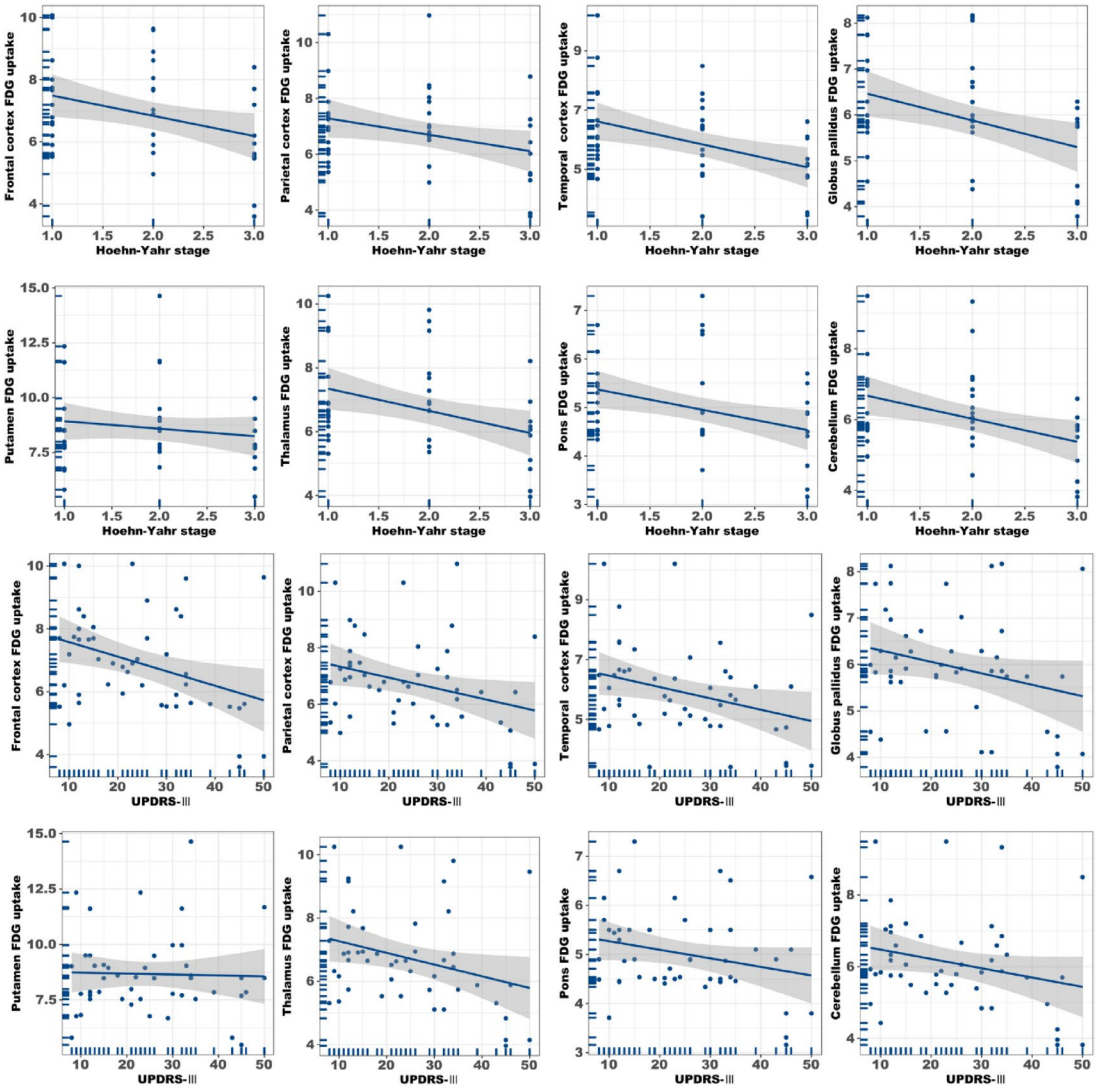

Fig. 2. The correlation between the FDG uptake and H&Y stages and UPDRS III score.

Region	PD	HC	*t* / *Z*	*P*
Caudate	14.083 ± 32.08	54.261 ± 22.31	− 8.046	< 0.0001*
Putamen	4.835 ± 31.13	42.009 ± 29.11	− 6.662	< 0.0001*
Globus pallidus	2.912 ± 44.05	66.182 ± 43.35	− 6.652	< 0.0001*
Substantia nigra	− 22.105 ± 43.67	0.703 ± 65.33	− 2.132	0.035*
Red nucleus	− 17.459 ± 33.60	29.720 ± 40.05	− 6.091	< 0.0001*

Table 3. Comparative analysis of the SWI phase values in HC individuals and patients with PD. The data are presented as mean ± standard deviation. HC, healthy control; PD, Parkinson's disease. *Statistically significant with $P < 0.05$.

FDG hypometabolism reflects synaptic dysfunction within the cortical-basal ganglia-thalamic network[25,26], as evidenced by the negative correlation between frontal cortex metabolism and UPDRS III scores ($r = -0.364$, $P = 0.011$). In contrast, reduced SWI phase values in the substantia nigra indicate iron-mediated oxidative stress, with a strong correlation to Hoehn-Yahr (H-Y) stages ($r = -0.525$, $P < 0.001$).

Second, the dynamic interplay between these two imaging modalities may mirror the cascading pathology of PD[27,28]. Cortical hypometabolism, such as that observed in the temporal lobe ($r = -0.405$), likely precedes iron-induced structural damage in the basal ganglia. This sequence aligns with Braak staging theory, which proposes that α-synuclein pathology spreads from the brainstem to the cortex[29]. Notably, putamen hypermetabolism ($r = -0.146$, $P = 0.318$) showed no correlation with clinical scores, suggesting compensatory metabolic

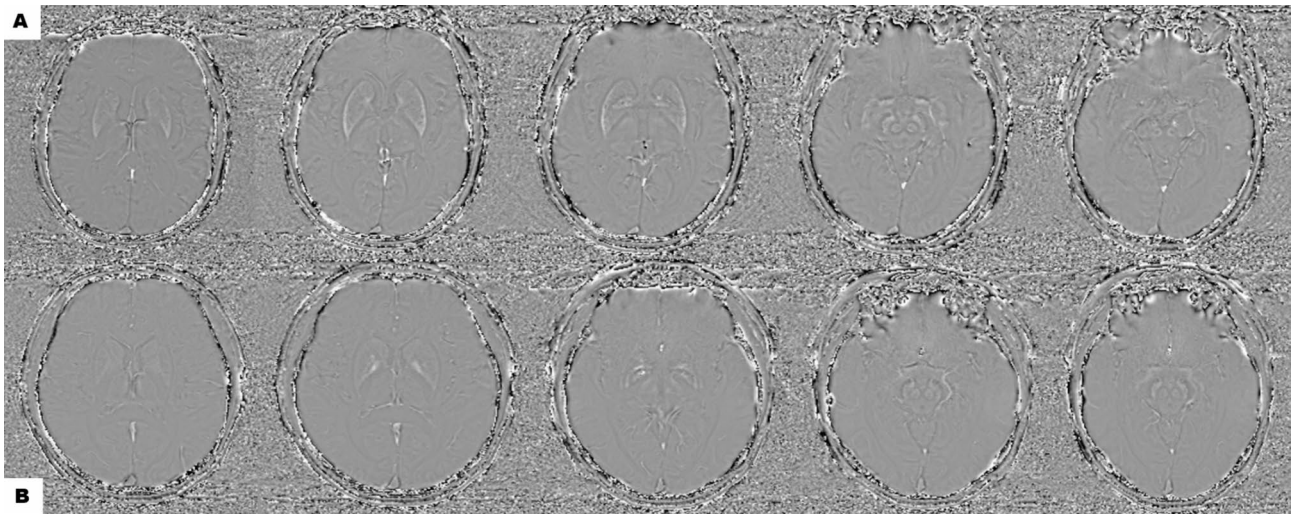

Fig. 3. The images presented the SWI of an HC individual (**A**) and a patient with PD (**B**). (**A**) HC group individual, man, 68 years. The SWI clearly shows the bilateral caudate, putamen, globus pallidus, substantia nigra, and red nucleus, with no obvious abnormal signals. (**B**) A 74-year-old male with PD. The SWI revealed signal reduction in the bilateral caudate, putamen, globus pallidus, substantia nigra, and red nucleus caused by iron deposition.

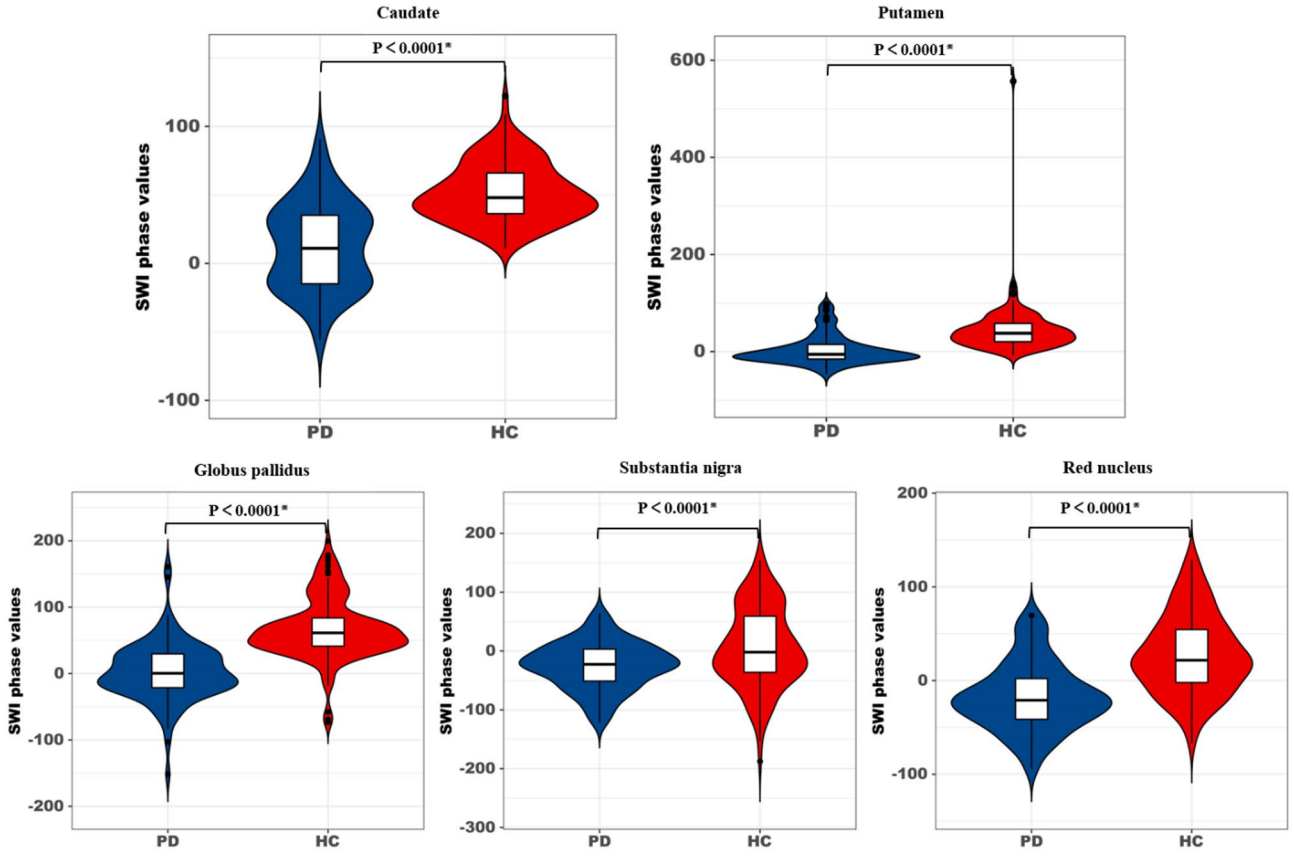

Fig. 4. Comparative analysis of phase values for both the PD and HC subjects in the SWI imaging. HC, healthy control; PD, Parkinson's disease; ASI, asymmetry index.

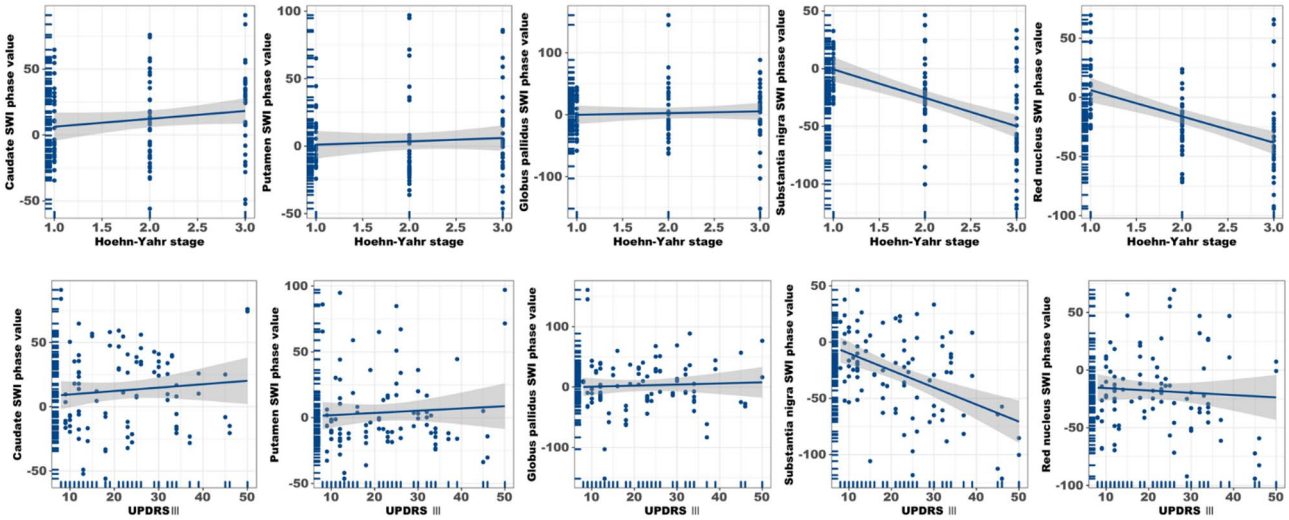

Fig. 5. The correlation between the SWI phase values and H&Y stages and UPDRS III score.

upregulation independent of motor symptom progression[30,31]. This finding is consistent with recent fMRI studies on basal ganglia functional reorganization[32].

Heterogeneity of imaging biomarkers and challenges in clinical translation

Despite significant correlations between iron deposition (reduced phase values) in the substantia nigra/red nucleus and disease staging, no such associations were observed in the globus pallidus or caudate ($P > 0.05$). This spatial heterogeneity may stem from PD subtype variations: for instance, postural instability/gait difficulty (PIGD) subtypes often exhibit more extensive basal ganglia iron deposition[33–35], whereas our cohort, likely dominated by tremor-dominant (TD) subtypes, may obscure region-specific correlations. Furthermore, SWI phase quantification is susceptible to magnetic field inhomogeneity[36]. Although high-resolution 1 mm slice thickness was employed, the absence of phase unwrapping correction may introduce measurement errors[37–39]. These technical limitations highlight the need for advanced iron quantification methods, such as quantitative susceptibility mapping (QSM), to enhance biomarker reproducibility[40,41].

Potential mechanisms underlying metabolic-iron interactions

Thalamic hypermetabolism ($Z = -2.020$, $P = 0.043$) showed no correlation with iron deposition, while pontine metabolic abnormalities ($Z = -3.637$, $P < 0.0001$) lacked interaction with SWI parameters. This may reflect functional independence within PD pathological networks: thalamic hypermetabolism could arise from compensatory activation due to reduced basal ganglia output[42], whereas pontine changes might relate to disinhibition in cerebellar-pontine-cortical circuits[43]. Crucially, the improved diagnostic performance of the multimodal model stems from orthogonal complementarity rather than direct biological interaction between biomarkers—a finding that supports machine learning strategies (e.g., ensemble learning) for weighted integration of heterogeneous features.

Limitations

Despite advances in multimodal integration, this study has several limitations. First, sample selection bias may have influenced the results. PD patients were not molecularly subtyped (e.g., α-synuclein PET subtypes) or pathologically confirmed, which risks the inclusion of atypical parkinsonism cases. Second, technical constraints were evident in the imaging analyses. SWI phase values are confounded by paramagnetic substances (e.g., calcifications) and lacked normalization to standardized reference regions. Additionally, PET analyses did not control for partial volume effects from cerebral atrophy. Third, the cross-sectional design of the study precludes elucidation of temporal relationships, such as whether compensatory hypermetabolism precedes iron-driven neuronal loss. Finally, clinical feasibility remains a concern. The cost and radiation exposure of multimodal protocols may limit their clinical adoption, necessitating streamlined AI-driven models for metabolic-iron mapping.

Conclusions and future directions

By innovatively combining ^{18}F-FDG PET and SWI, this study reveals the complementary value of multimodal imaging biomarkers and establishes a generalizable diagnostic framework. Future research should focus on: (1) integrating tau-PET and QSM to dissect tripartite interactions among α-synuclein pathology, iron deposition, and metabolic dysregulation; (2) developing deep learning-based multimodal fusion algorithms to enhance early diagnostic sensitivity; and (3) conducting multicenter longitudinal cohorts to link imaging biomarkers with disease-modifying therapeutic outcomes. These efforts will advance PD management toward personalized and precision medicine.

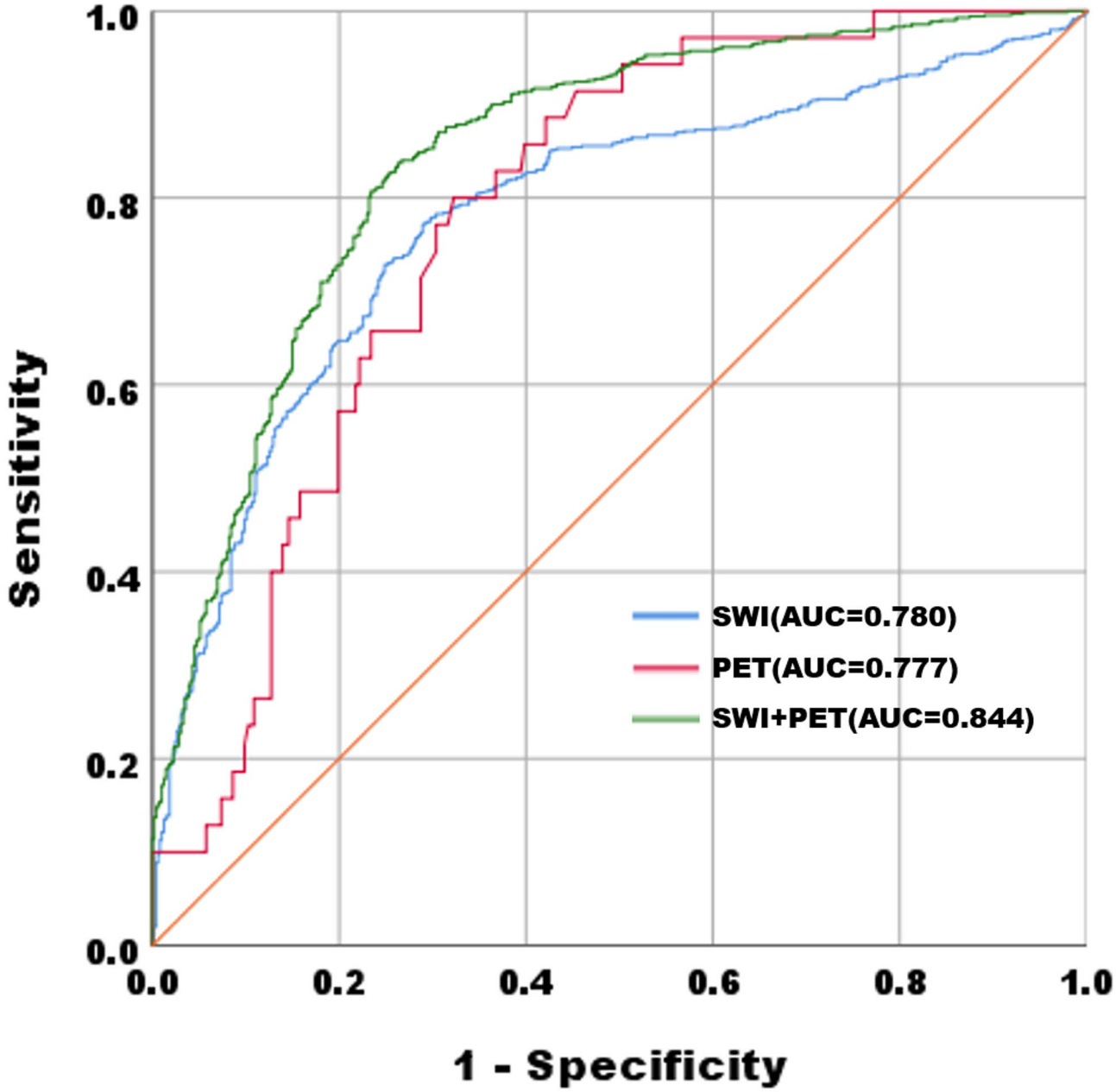

Fig. 6. ROC curve analysis of the ^{18}F-FDG PET, SWI model and PET + SWI model in differentiating early PD from HC.

Data availability

The datasets used and/or analysed during the current study available from the corresponding author on reasonable request.

Received: 18 March 2025; Accepted: 15 May 2025
Published online: 06 June 2025

References

1. Tolosa, E., Garrido, A., Scholz, S. W. & Poewe, W. Challenges in the diagnosis of Parkinson's disease. *Lancet Neurol.* **20**, 385–397. https://doi.org/10.1016/s1474-4422(21)00030-2 (2021).
2. Li, L. et al. A Mendelian randomization study on association of alpha-synuclein and GPNMB with Parkinson's disease risk and progression. *Mol. Neurobiol.* https://doi.org/10.1007/s12035-025-04928-z (2025).
3. Jankovic, J. & Tan, E. K. Parkinson's disease: Etiopathogenesis and treatment. *J. Neurol. Neurosurg. Psychiatry* **91**, 795–808. https://doi.org/10.1136/jnnp-2019-322338 (2020).
4. Masato, A., Plotegher, N., Boassa, D. & Bubacco, L. Impaired dopamine metabolism in Parkinson's disease pathogenesis. *Mol. Neurodegener.* **14**, 35. https://doi.org/10.1186/s13024-019-0332-6 (2019).

5. Munhoz, R. P., Tumas, V., Pedroso, J. L. & Silveira-Moriyama, L. The clinical diagnosis of Parkinson's disease. *Arq. Neuropsiquiatr.* **82**, 1–10. https://doi.org/10.1055/s-0043-1777775 (2024).
6. Burtscher, J. et al. Exercise and gait/movement analyses in treatment and diagnosis of Parkinson's Disease. *Ageing Res. Rev.* **93**, 102147. https://doi.org/10.1016/j.arr.2023.102147 (2024).
7. Beach, T. G. & Adler, C. H. Importance of low diagnostic accuracy for early Parkinson's disease. *Mov. Disord. Off. J. Mov. Disord. Soc.* **33**, 1551–1554. https://doi.org/10.1002/mds.27485 (2018).
8. Jeong, S. H. et al. Association of choroid plexus volume with motor symptoms and dopaminergic degeneration in Parkinson's disease. *J. Neurol. Neurosurg. Psychiatry* **94**, 1047–1055. https://doi.org/10.1136/jnnp-2023-331170 (2023).
9. Armstrong, M. J. & Okun, M. S. Diagnosis and treatment of Parkinson disease: A review. *JAMA* **323**, 548–560. https://doi.org/10.1001/jama.2019.22360 (2020).
10. Tian, M. et al. International consensus on clinical use of presynaptic dopaminergic positron emission tomography imaging in parkinsonism. *Eur. J. Nucl. Med. Mol. Imaging* **51**, 434–442. https://doi.org/10.1007/s00259-023-06403-0 (2024).
11. Booth, S., Park, K. W., Lee, C. S. & Ko, J. H. Predicting cognitive decline in Parkinson's disease using FDG-PET-based supervised learning. *J. Clin. Investig.* https://doi.org/10.1172/jci157074 (2022).
12. Seo, S. et al. Striatal dopamine transporter uptake predicts neuronal hypometabolism and visuospatial function in Parkinson's disease. *Eur. J. Nucl. Med. Mol. Imaging* https://doi.org/10.1007/s00259-025-07137-x (2025).
13. Weng, R. et al. The cerebellar glucose metabolism in moyamoya vasculopathy and its correlation with neurocognitive performance after cerebral revascularization surgery: A [(18)F]FDG PET study. *Eur. J. Nucl. Med. Mol. Imaging* **52**, 1520–1534. https://doi.org/10.1007/s00259-024-06995-1 (2025).
14. Hu, X. et al. Multivariate radiomics models based on (18)F-FDG hybrid PET/MRI for distinguishing between Parkinson's disease and multiple system atrophy. *Eur. J. Nucl. Med. Mol. Imaging* **48**, 3469–3481. https://doi.org/10.1007/s00259-021-05325-z (2021).
15. Schröter, N. et al. Nigral glucose metabolism as a diagnostic marker of neurodegenerative parkinsonian syndromes. *NPJ Parkinson's Dis.* **8**, 123. https://doi.org/10.1038/s41531-022-00392-x (2022).
16. Brumberg, J. et al. [(18)F]Florzolotau PET for the differential diagnosis of Parkinsonism in patients with suspected 4-repeat tauopathies. *J. Nucl. Med.* https://doi.org/10.2967/jnumed.124.268956 (2025).
17. Carli, G. et al. Parkinson's disease-related pattern in isolated REM sleep behaviour disorder as a prodromal progression marker: 8-year follow-up changes assessed at three time points. *Eur. J. Nucl. Med. Mol. Imaging* https://doi.org/10.1007/s00259-025-07260-9 (2025).
18. Haller, S., Haacke, E. M., Thurnher, M. M. & Barkhof, F. Susceptibility-weighted imaging: Technical essentials and clinical neurologic applications. *Radiology* **299**, 3–26. https://doi.org/10.1148/radiol.2021203071 (2021).
19. Hamed, M. R. et al. Fast susceptibility-weighted imaging using echo planar imaging at 1.5 T for swallow tail sign biomarker detection in Parkinson's disease. *Radiography* **31**, 102903. https://doi.org/10.1016/j.radi.2025.102903 (2025).
20. Pillai, K. S. et al. Multimodality brain imaging markers in progressive supranuclear palsy subtypes and Parkinson's disease. *Mov. Disord. Clin. Pract.* https://doi.org/10.1002/mdc3.14346 (2025).
21. Sun, J. et al. Identification of Parkinson's disease and multiple system atrophy using multimodal PET/MRI radiomics. *Eur. Radiol.* **34**, 662–672. https://doi.org/10.1007/s00330-023-10003-9 (2024).
22. Postuma, R. B. et al. Validation of the MDS clinical diagnostic criteria for Parkinson's disease. *Mov. Disord. Off. J. Mov. Disorder Soc.* **33**, 1601–1608. https://doi.org/10.1002/mds.27362 (2018).
23. Hong, Y. et al. Delayed (18)F-FDG PET imaging provides better metabolic asymmetry in potential epileptogenic zone in temporal lobe epilepsy. *Front. Med.* **10**, 1180541. https://doi.org/10.3389/fmed.2023.1180541 (2023).
24. Zang, Z. et al. Modulation effect of substantia nigra iron deposition and functional connectivity on putamen glucose metabolism in Parkinson's disease. *Hum. Brain Mapp.* **43**, 3735–3744. https://doi.org/10.1002/hbm.25880 (2022).
25. He, S., Everest-Phillips, C., Clouter, A., Brown, P. & Tan, H. Neurofeedback-linked suppression of cortical β bursts speeds up movement initiation in healthy motor control: A double-blind sham-controlled study. *J. Neurosci. Off. J. Soc. Neurosci.* **40**, 4021–4032. https://doi.org/10.1523/jneurosci.0208-20.2020 (2020).
26. Shen, Z. et al. Cross-modality PET image synthesis for Parkinson's Disease diagnosis: A leap from [(18)F]FDG to [(11)C]CFT. *Eur. J. Nucl. Med. Mol. Imaging* https://doi.org/10.1007/s00259-025-07096-3 (2025).
27. Yoon, R. G. et al. The utility of susceptibility-weighted imaging for differentiating Parkinsonism-predominant multiple system atrophy from Parkinson's disease: correlation with 18F-flurodeoxyglucose positron-emission tomography. *Neurosci. Lett.* **584**, 296–301. https://doi.org/10.1016/j.neulet.2014.10.046 (2015).
28. Chen, B. et al. Metabolic network connectivity disturbances in Parkinson's disease: a novel imaging biomarker. *Cerebral cortex* https://doi.org/10.1093/cercor/bhae355 (2024).
29. Nakano, Y., Niethammer, M. & Eidelberg, D. Imaging of disease-related networks in Parkinson's disease. *Cold Spring Harb. Perspect. Med.* https://doi.org/10.1101/cshperspect.a041841 (2025).
30. Leng, F. et al. Iron deposition is associated with motor and non-motor network breakdown in parkinsonism. *Front. Aging Neurosci.* **16**, 1518155. https://doi.org/10.3389/fnagi.2024.1518155 (2024).
31. Zhao, H., Ji, Q. H., Jia, Z. Z. & Shen, L. H. Association between deep gray matter iron deposition and clinical symptoms in Parkinson's disease: A quantitative susceptibility mapping study. *Front. Neurol.* **15**, 1442903. https://doi.org/10.3389/fneur.2024.1442903 (2024).
32. Rebelo, D. et al. A link between synaptic plasticity and reorganization of brain activity in Parkinson's disease. *Proc. Natl. Acad. Sci. USA* https://doi.org/10.1073/pnas.2013962118 (2021).
33. Ying, C. C. et al. Correlation between substantia nigra hyperechogenicity and iron metabolism in the postural instability gait difficulty subtype of Parkinson's disease. *Ultrasound Med. Biol.* **49**, 2422–2427. https://doi.org/10.1016/j.ultrasmedbio.2023.08.010 (2023).
34. Boonstra, J. T., Michielse, S., Temel, Y., Hoogland, G. & Jahanshahi, A. Neuroimaging detectable differences between Parkinson's disease motor subtypes: A systematic review. *Mov. Disord. Clin. Pract.* **8**, 175–192. https://doi.org/10.1002/mdc3.13107 (2021).
35. Zhang, X. et al. Distribution pattern of iron deposition in the basal ganglia of different motor subtypes of Parkinson's disease. *Neurosci. Lett.* **807**, 137249. https://doi.org/10.1016/j.neulet.2023.137249 (2023).
36. Wang, C. et al. Enhancing nigrosome-1 sign identification via interpretable AI using true susceptibility weighted imaging. *J. Magn. Resonance Imaging JMRI* **60**, 1904–1915. https://doi.org/10.1002/jmri.29245 (2024).
37. Sotoudeh, H. et al. Susceptibility-weighted imaging in neurodegenerative disorders: A review. *J. Neuroimaging Off. J. Am. Soc. Neuroimaging* **31**, 459–470. https://doi.org/10.1111/jon.12841 (2021).
38. Su, D. et al. Distinctive pattern of metal deposition in neurologic Wilson disease: Insights from 7T susceptibility-weighted imaging. *Neurology* **102**, e209478. https://doi.org/10.1212/wnl.0000000000209478 (2024).
39. Mohammadi, S. & Ghaderi, S. Parkinson's disease and Parkinsonism syndromes: Evaluating iron deposition in the putamen using magnetic susceptibility MRI techniques—a systematic review and literature analysis. *Heliyon* **10**, e27950. https://doi.org/10.1016/j.heliyon.2024.e27950 (2024).
40. Yang, Y. et al. Utilizing combined quantitative multiparametric MRI as potential biomarkers for improved early-stage parkinson's disease diagnosis. *Neurol. Sci. Off. J. Italian Neurol. Soc. Italian Soc. Clin. Neurophysiol.* https://doi.org/10.1007/s10072-024-07956-0 (2024).
41. Suh, P. S. et al. Deep learning-based algorithm for automatic quantification of nigrosome-1 and Parkinsonism classification using susceptibility map-weighted MRI. *AJNR Am. J. Neuroradiol.* https://doi.org/10.3174/ajnr.A8585 (2024).

42. Molinet-Dronda, F. et al. Cerebral metabolic pattern associated with progressive parkinsonism in non-human primates reveals early cortical hypometabolism. *Neurobiol. Dis.* **167**, 105669. https://doi.org/10.1016/j.nbd.2022.105669 (2022).
43. Diao, Y. et al. Abnormal neuronal activity in the subthalamic nucleus contributes to dysarthria in patients with Parkinson's disease. *Neurobiol. Dis.* **207**, 106830. https://doi.org/10.1016/j.nbd.2025.106830 (2025).

Author contributions
Z.H. and C.Y. and S.L. wrote the main manuscript text and L.Z. and S.L. prepared Figs. 1–3. All authors reviewed the manuscript.

Funding
Hubei Province Key Laboratory of Molecular Imaging, 2024fzyx020, 2024fzyx020, 2024fzyx020, 2024fzyx020, Institution-Level Science and Technology Innovation Project, XYY2025QN09, XYY2025QN09, XYY2025QN09, XYY2025QN09.

Declarations

Competing interests
The authors declare no competing interests.

Additional information
Correspondence and requests for materials should be addressed to S.L.

Reprints and permissions information is available at www.nature.com/reprints.

Publisher's note Springer Nature remains neutral with regard to jurisdictional claims in published maps and institutional affiliations.